Electronic Supplementary Material (ESI) for Journal of Materials Chemistry C.

Supplementary Information for

Tailoring anisotropic thermal conductivity of 2D aramid nanoribbons-based dielectrics with potential high-temperature capacitive energy storage

Xiang Yu,[a,b] Rui Yang,[a] Guangyi Shen[a], Kaixuan Sun,[a] Fangcheng Lv,[a,b] and Sidi Fan[a,b]*

[a]*School of Electrical and Electronic Engineering, North China Electric Power University, Beijing 102206, China*

[b]*State Key Laboratory of Alternate Electrical Power System with Renewable Energy Sources, North China Electric Power University, Beijing 102206, China*

* Corresponding author.

E-mail: sidifan@ncepu.edu.cn

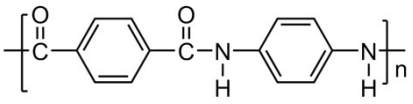

Figure S1. Chemical structure of *p*-phenylene terephthalamide (PPTA).

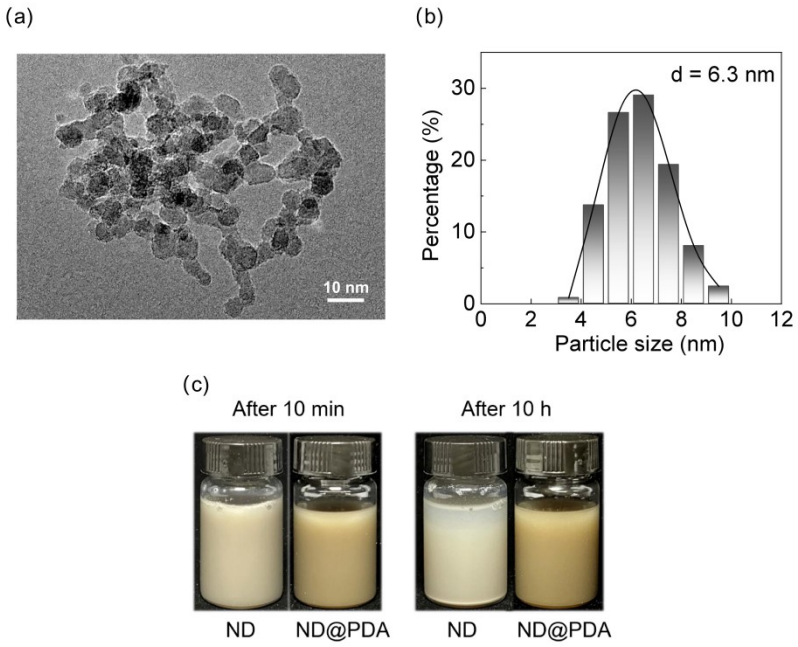

Figure S2. (a) SEM image of ND particles. (b) Statistical analysis of the diameter distribution of ND particles. (c) Comparison of dispersion states of ND and ND@PDA aqueous solutions observed after 10 min and after 10 h of standing.

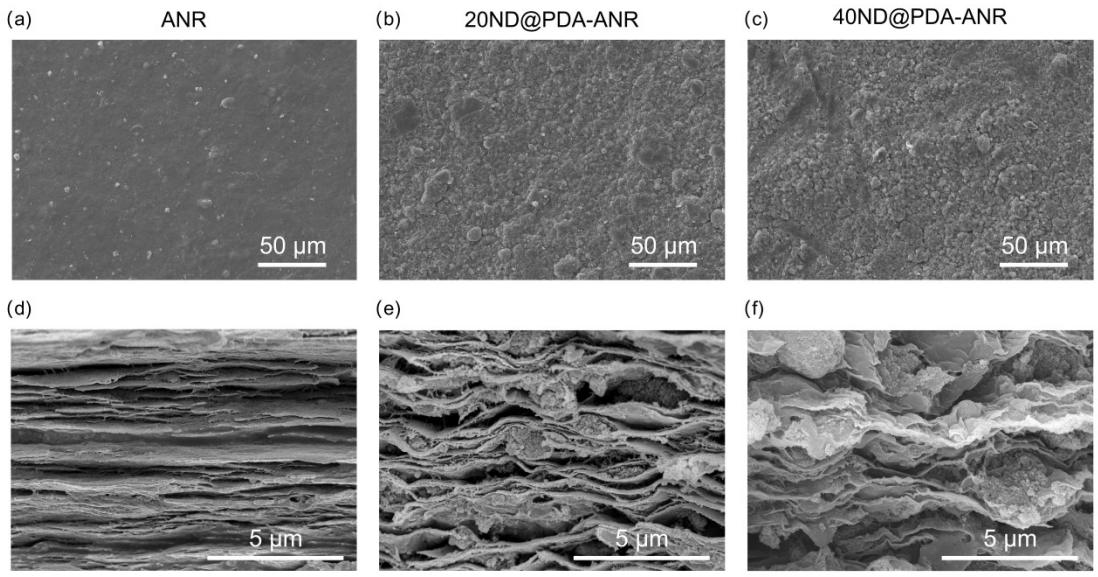

Figure S3. Surface morphology of (a) ANR, (b) 20ND@PDA-ANR, and (c) 40ND@PDA-ANR films. Cross-sectional morphology of (d) ANR, (e) 20ND@PDA-ANR, and (f) 40ND@PDA-ANR films.

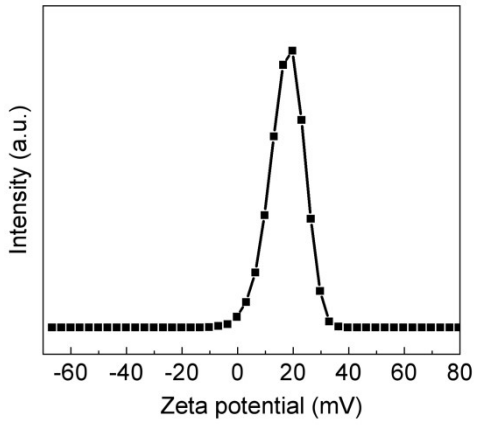

Figure S4. *Zeta* potential distribution analysis of ND@PDA particles.

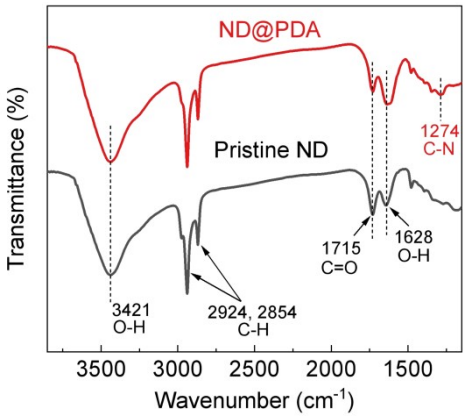

Figure S5. FTIR spectra of pristine ND and ND@PDA particles. Strong absorption peaks at 3421 cm^{-1} and 1628 cm^{-1} are assigned to stretching vibration and bending vibration of O-H, respectively, which stem from the absorbed water molecules on the ND surface. The peaks at 2924 cm^{-1} and 2854 cm^{-1} are consistent with stretching vibration of C-H functional groups. The peak centered at 1715 cm^{-1} represents stretching band of C=O functional groups.

Note 1. Modified Hashin-Shtrikman model for fitting thermal conductivity values

The modified Hashin-Shtrikman model is employed to determine the thermal boundary resistance in our composite films, fitting the experimental thermal conductivity values by,

$$k_{\mathrm{com}} = k_{\mathrm{m}} \frac{1 + 2k\sum_{i=1}^{n} V_{\mathrm{i}} E_{\mathrm{i}}}{1 - k\sum_{i=1}^{n} V_{\mathrm{i}} E_{\mathrm{i}}} \tag{1}$$

$$K = 13.3347 \exp(-13.2701 R_{\mathrm{c}}) \tag{2}$$

$$E_i = \frac{\frac{k_{\mathrm{f}}}{k_{\mathrm{m}}} - 1}{\frac{k_{\mathrm{f}}}{k_{\mathrm{m}}} + 1} \tag{3}$$

$$V_{\mathrm{i}} = \frac{1}{1 + \frac{(1 - wt)/wt}{\rho_{\mathrm{m}} / \rho_{\mathrm{f}}}} \tag{4}$$

where k_{com}, k_{m}, and k_{f} are the thermal conductivity of the composite, matrix, and filler, respectively. n is the number of filler species (n = 1 in this work), V_{i} is the volume fraction of fillers, wt is the weight fraction of fillers, ρ_{f} and ρ_{m} is the density of filler and matrix, respectively. The empirical equation of K is related to the total thermal resistance of composites, with R_{c} representing the determined thermal boundary resistance. In this work, the $k_{\perp}$ and $k_{//}$ values of the ANR matrix are 0.08 W/(m·K) and 1.86 W/(m·K), respectively. The thermal conductivity of ND is 2000 W/(m·K). The ρ_{f} and ρ_{m} values are 1.8 g/cm^3 and 0.96 g/cm^3, respectively.

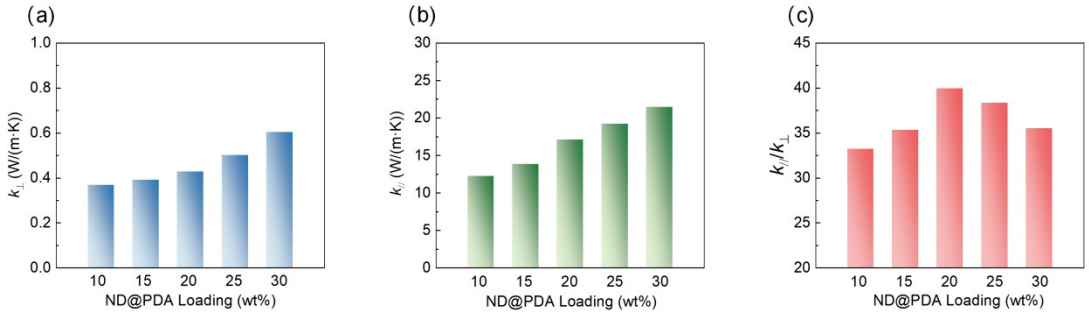

Figure S6. (a) Out-of-plane ($k_{\perp}$) and (b) in-plane ($k_{//}$) thermal conductivity of various samples. (c) The anisotropic ratio ($k_{//}/k_{\perp}$) as a function of filler loading ratio.

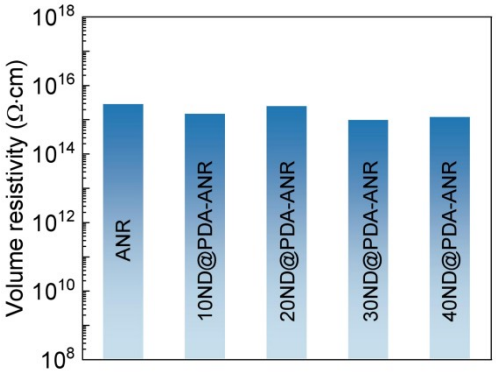

Figure S7. Volume electrical resistivity of various samples.

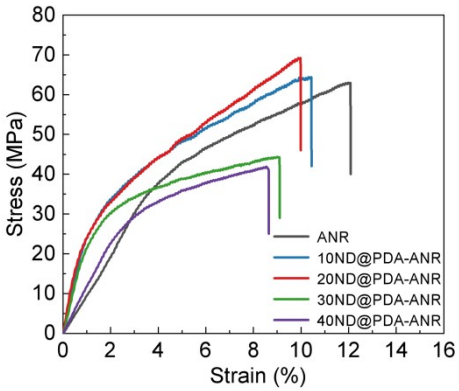

Figure S8. Tensile strength-elongation curves measured for samples at different filler loading ratio.

Note 2. Electric-thermal-mechanical coupling models for phase field simulations

The models are constructed by the cooperation of MATLAB and COMSOL Multiphysics, following the coding flow diagram as shown in Figure S9.

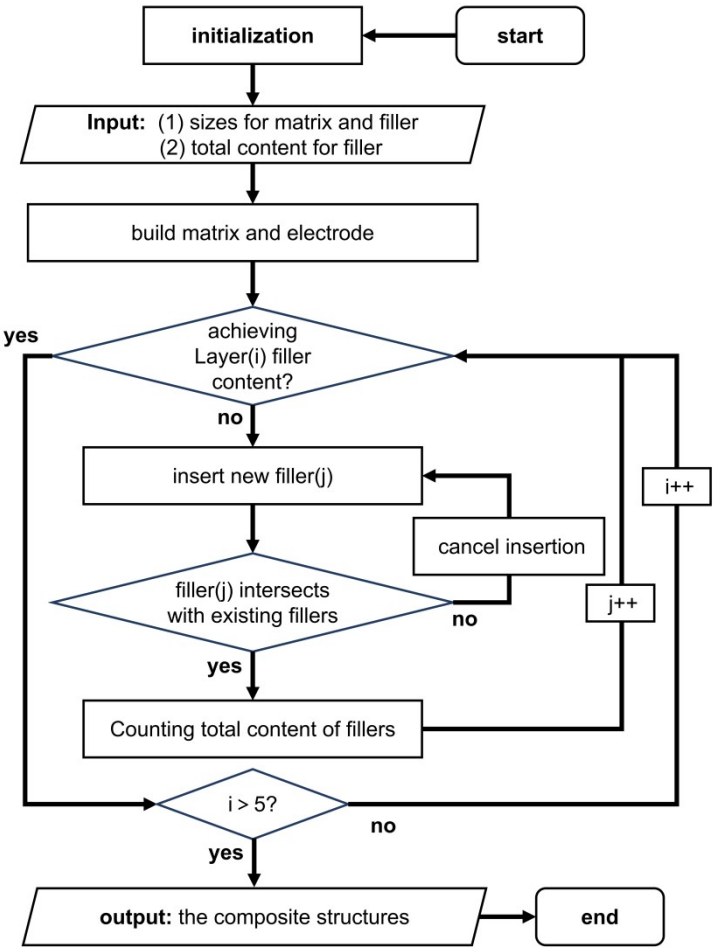

Figure S9. The code diagram of model construction.

Figure S10 shows the models constructed for phase field (PF) simulation. First, rectangular matrix of ANR is set up with desired sizes. In the composite model, spherical fillers are added layer-by-layer along the in-plane direction at an appointed loading ratio. The addition of each new filler is judged by the traversal method to decide whether it intersects with already existing fillers and whether it is inside specified layer. After passing the judgment, it is recorded in the packing set, and its mass is counted in the total content of fillers. When the total content of the packing exceeds the amount of packing loading, the output model of final composite system with a certain amount of loading is obtained.

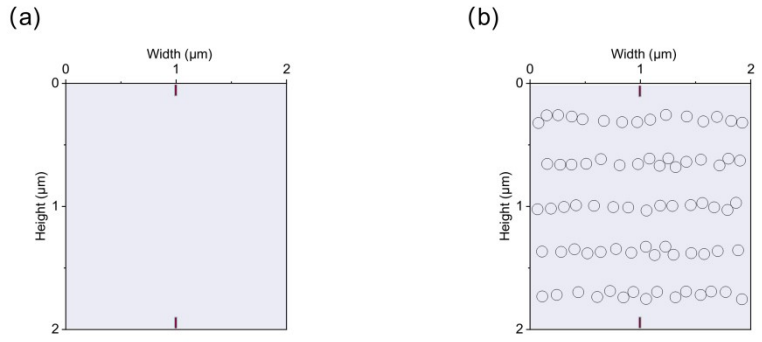

Figure S10. The models constructed for phase field simulations.

To simulate the dielectric breakdown, a continuous PF variable $\eta(r,t)$ is introduced to describe the evolution of breakdown phase. In a certain region, the value of $\eta(r,t)$ gradually decreases from 1 to 0, representing a gradual transition from intact state to complete breakdown state. The electric and thermal stimuli are simultaneously considered for investigating their effects on the breakdown process. Synergistic contributions from phase separation, interface, temperature and electric field are considered for free energy in a dielectric inhomogeneous system, written as,

$$F = \int_V [f_{tol}(r)]dV \tag{5}$$

where $f_{tol}(r)$ is the total energy density which is constituted by,

$$f_{tol}(r) = f_{sep}(\eta(r)) + f_{grad}(\eta(r)) + f_{elec}(r) + f_{joule}(r) + f_{strain}(r) \tag{6}$$

where in the integral, the first term represents free energy density of mixing that drives the phase separation, the second term is gradient energy density, the third term is electric energy density, the fourth term is Joule heat energy density, and the last term is strain energy density, separately described by,

$$f_{sep}(\eta(r)) = \alpha\eta^2(1-\eta)^2 \tag{7}$$

where α is a positive coefficient defining the energy barrier of phase separation.

$$f_{grad}(\eta(r)) = -\frac{1}{2}\gamma|\nabla\eta(r)|^2 \tag{8}$$

where γ is the gradient energy coefficient in isotropic approximation.

$$f_{elec}(r) = \frac{1}{2}\varepsilon_0\varepsilon_{ij}(r)E_i(r)E_j(r) + \frac{1}{2}E_i(r)P_i^S(r) \tag{9}$$

where $\varepsilon_{ij}(r)$ is the spatially dependent relative dielectric constant tensor, $E_i(r)$ is the total electric

field component, and $P_i^S(r)$ is the spontaneous polarization which is not zero if the local material component is ferroelectric.

$$f_{joule}(r) = \sigma_{ij}(r,T)E_i(r)E_j(r)dt \tag{10}$$

where $\sigma_{ij}(r,T)$ is the spatially and temperature dependent electrical conductivity tensor, and *dt* is the operating time of applied electric field.

$$f_{strain}(r) = \frac{\sigma_m^2}{2Y(r)} = \frac{\varepsilon_0^2\varepsilon_{ij}^2(r)E_i^2(r)E_j^2(r)}{8Y(r)} \tag{11}$$

where $Y(\mathbf{r})$ is the Young's modulus.

A modified Allen-Cahn equation is employed to describe the breakdown phase evolution,

$$\frac{\partial\eta(r,t)}{\partial t} = -L_0 H\left(f_{elec} + f_{joule} - f_{critical}\right)\frac{\partial f_{tol}(r)}{\partial\eta(r,t)} \tag{12}$$

where L_0 is the kinetic coefficient relating to the interface mobility with a value of 10^{-7} $m^2 \cdot s^{-1} \cdot N^{-1}$, $H\left(f_{elec} + f_{joule} - f_{critical}\right)$ is the Heaviside unit step function $\left(H\left(\left(f_{elec} + f_{joule} + f_{strain}(r)\right) < f_{critical}\right) = 0\right)$ and $\left(H\left(\left(f_{elec} + f_{joule} + f_{strain}(r)\right) > f_{critical}\right) = 1\right)$, and $f_{critical}$ is the critical energy of each component in the composite which is calculated by,

$$f_{critical} = \frac{1}{2}\varepsilon_0\varepsilon_r E_b^2 + \sigma E_b^2 dt + \frac{\varepsilon_0^2\varepsilon_r^2 E_b^4}{8Y} \tag{13}$$

In order to describe both matrix and fillers in the composite, a non-evolving field variable $\rho(r)$ is introduced, which is equal to 1 in fillers and equal to 0 in matrix. With this definition, the spatially dependent relative dielectric constant and electrical conductivity during the microstructure evolution process takes the form,

$$\begin{aligned}\varepsilon_{ij}(r) = {} & \eta^3\left(10-15\eta+6\eta^2\right)\varepsilon_{ij}^B + \left[1-\eta^3\left(10-15\eta+6\eta^2\right)\right]\times \\ & \left\{\rho^3\left(10-15\rho+6\rho^2\right)\varepsilon_{ij}^F + \left[1-\rho^3\left(10-15\rho+6\rho^2\right)\right]\varepsilon_{ij}^M\right\}\end{aligned} \tag{14}$$

$$\begin{aligned}\sigma_{ij}(r) = {} & \eta^3\left(10-15\eta+6\eta^2\right)\sigma_{ij}^B + \left[1-\eta^3\left(10-15\eta+6\eta^2\right)\right]\times \\ & \left\{\rho^3\left(10-15\rho+6\rho^2\right)\sigma_{ij}^F + \left[1-\rho^3\left(10-15\rho+6\rho^2\right)\right]\sigma_{ij}^M\right\}\end{aligned} \tag{15}$$

where ε_{ij}^B, ε_{ij}^F, ε_{ij}^M, σ_{ij}^B, σ_{ij}^F and σ_{ij}^M indicate the relative dielectric constant and electrical conductivity of the breakdown phase, filler, and matrix, respectively.

In order to obtain the electric field distribution during the microstructure evolution process, the

spectral iterative perturbation method is employed with the iterative equation in real space as following,

$$\sigma_{ij}^{ref}\frac{\partial^2\varphi^n(r)}{\partial r_i\partial r_j}=\frac{\partial}{\partial r_i}\left[\Delta\sigma_{ij}(r)E_j^{ext}\right] \tag{16}$$

with σ_{ij}^{ref} is a homogeneous reference of electrical conductivity, and $\Delta\sigma_{ij}(r)=\sigma_{ij}(r)-\sigma_{ij}^0$ is the inhomogeneous perturbation.

The settings of material parameters for PF model are shown in Table S1. The relative dielectric constant ε_{ij}^B and the electrical conductivity σ_{ij}^B of breakdown phase are considered to be isotropic and have a value of 10^4 and 1×10^{-4} S/m to reflect its abundant space charges in the breakdown region. The coefficient α in the separation energy term is given by a value of 10^8 J/m^3 to represent the barrier of breakdown phase and the non-breakdown phase. A value of 10^{-8} J/m is used for the gradient energy coefficient γ to specify d_0 10 nm in the modeling.

Table S1. The settings of material parameters for PF model

Material	Dielectric constant	Electrical conductivity (S/m)	Intrinsic breakdown strength E_b (kV/mm)	Density (g/cm^3)	Thermal conductivity (W/(m·K))	Young's modulus (GPa)
ND filler	6	10^{-16}	1200	3.3	2000	2.1
PPTA matrix	3	10^{-14}	200	1.27	0.22	1000

Note 3. Distributions of strain energy density

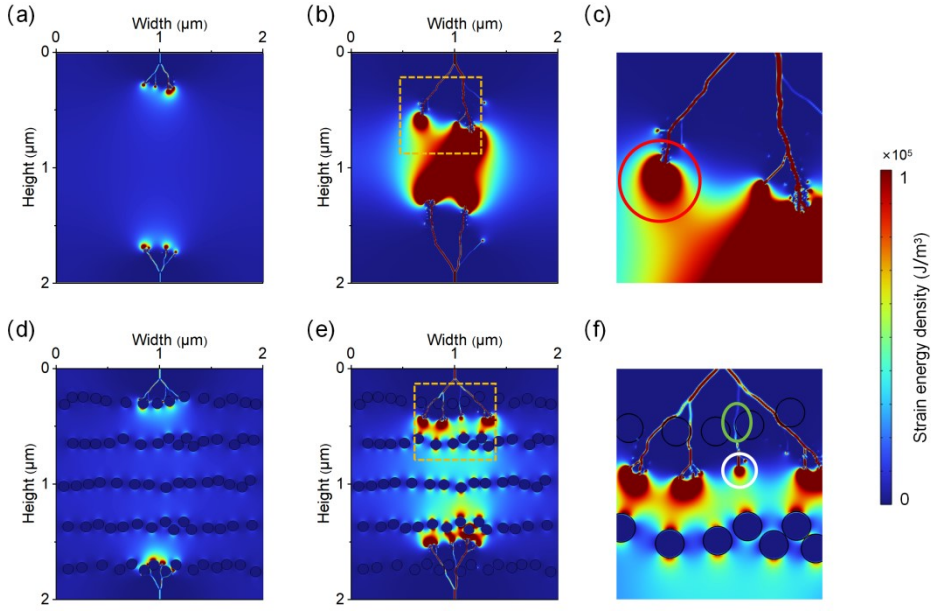

Figure S11. (a) The strain energy density in the pristine model at 45 ms, and (b) at 75 ms, along with (c) an enlarged view of 75 ms. (d) The strain energy density in the composite model at 45 ms, and (d) at 75 ms, along with (f) an enlarged view of 75 ms.

It is evident that electrical trees in the two models present different strain energy distributions, which can be ascribed to the following two aspects.

(1) Effective strain energy dissipation. In the pristine model (see Figure S11b), the entire electrical tree presents a deep red color, representing the presence of high strain energy within the electrical tree. This poses a threat to the dielectric film, potentially leading to the mechanical breakdown originating from internal locations. In contrast, the electric tree in the composite model demonstrates a distinct appearance, with certain branches near ND fillers displaying a blue color (see Figure S11f with the green circle), signifying reduced strain energy. This can be attributed to the high stiffness of ND fillers, allowing the effective dissipation of high strain energy from the electrical tree to ND fillers during the electrical deformation. This, in turn, helps to prevent the composite film from enduring high strain stress and potential breakdown risks.

(2) Reduced strain energy at the tips of the electrical tree. In the pristine model, without effective exchange of strain energy exchange between the electrical tree and ND fillers, high strain energy is concentrated at the tips of the electrical tree (see Figure S11c with the red circle). The

strained regions expand and tend to connect with neighboring area, thus subjecting the entire film to high strain stress. Under high strain energy, the mechanical deformation facilitates the growth of the electrical tree without encountering any obstacles. On the contrary, with an effective exchange of strain energy, the strain stress at the tips is significantly released, resulting limited strained regions (see Figure S11c with the white circle). Therefore, the potential for mechanical deformation is reduced that slows down the growth of the electrical tree.

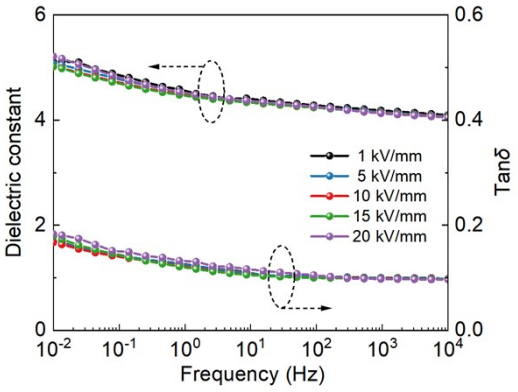

Figure S12. Frequency-dependent dielectric constant and dielectric loss at different electric fields.

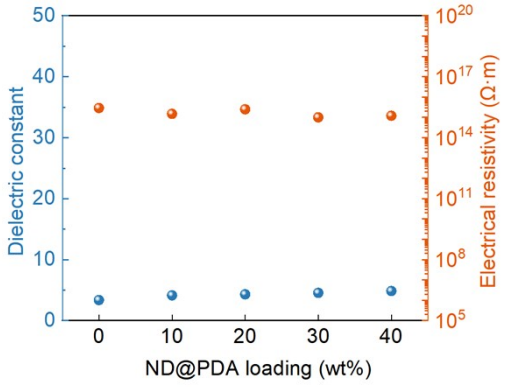

Figure S13. Dielectric constant (1 kHz) and electrical resistivity as a function of the filler doping concentration.

Note 4. Temperature-dependent dielectric performance

The temperature-dependent dielectric properties, specifically the dielectric constant and dielectric loss (tanδ) are presented in Figure S14. The measurements are performed at a fixed frequency of 1 kHz. As illustrated in Figure S14a, the dielectric constant of the pristine film exhibits a gradual increase with rising temperature. Upon doping with ND@PDA fillers, all the composite films demonstrate remarkable stability in their dielectric constant across the entire temperature range, indicating the effectiveness of fillers in stabilizing this property. On the other hand, Figure S14b reveals a picture of the dielectric loss behavior. At lower doping ratios of 10 wt% and 20 wt%, the tanδ values remain well-controlled, staying below 0.1 up to 200°C. However, as the doping ratio increases to 30 wt% and 40 wt%, a sharp rise in tanδ is observed with increasing temperature. This increase is attributed to the aggregation of excessive fillers, which leads to structural deformation and weakened interfacial interactions. Consequently, the confinement of interface molecular chains is reduced, and thermally activated relaxation oculus at higher temperatures, resulting in enhanced dielectric loss.

In balancing the trade-off between dielectric constant and dielectric loss, it is evident that a doping ratio of 20 wt% offers an optimal solution. This ratio not only maintains a stable dielectric constant but also keeps the dielectric loss low, thereby enhancing the overall energy storage efficiency.

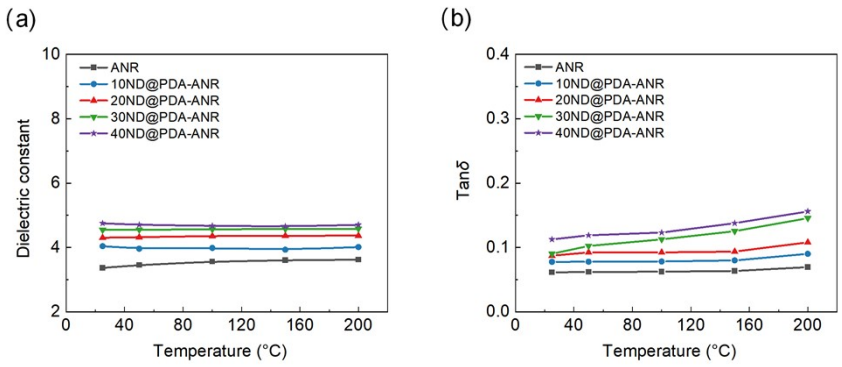

Figure S14. (a) Temperature-dependent dielectric constant, and (b) dielectric loss of various samples.

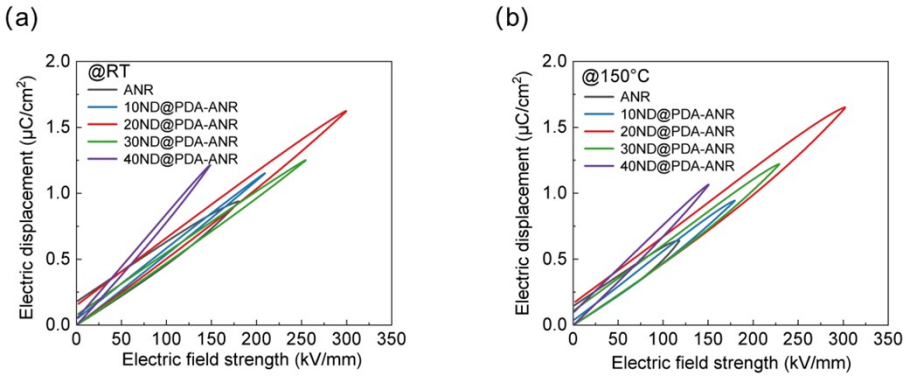

Figure S15. (a) *D–E* loops of various samples at room temperature, and (b) at 150°C.

Note 5. Temperature-dependent breakdown strength and energy storage parameters

The breakdown strength is a crucial determinant for high-temperature energy storage capacity. It effectively indicates the maximum tolerable electric field that can be applied without causing failure. The temperature-dependent breakdown strength is shown in Figure S16. A clear downward trend in breakdown strength is revealed as the temperature rises. At 150°C, it remains above 300 kV/mm, exhibiting a remarkably controlled decrease of just 2.9% compared to the value at ambient temperature. While it experiences a more rapid degradation to 283 kV/mm at 200°C, this decrease still falls within a 10% range, indicating a relatively good stability in breakdown strength despite temperature fluctuations.

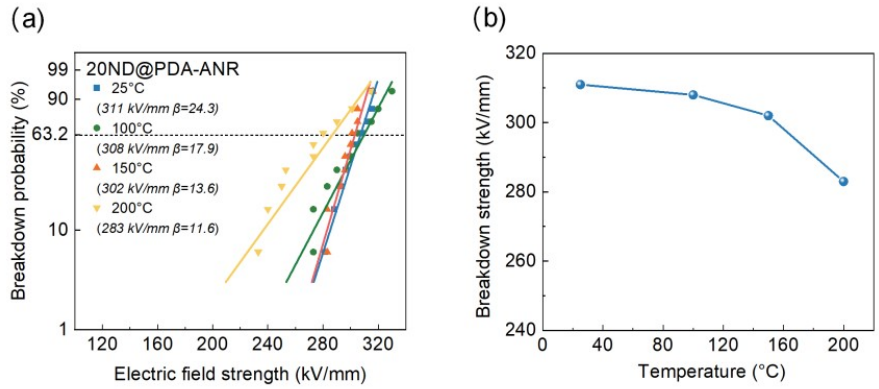

Figure S16. (a) Temperature-dependent Weibull distribution plots and (b) characteristic breakdown strength of 20ND@PDA-ANR.

The temperature-dependent energy storage parameters, including U_e and η, are displayed in Figure S17. During the energy storage test, the electric field applied to the 20ND@PDA-ANR film is determined based on the characteristic breakdown strength illustrated in Figure S16. The electric field is set at 300 kV/mm for 25°C, 100°C, and 150°C, while a slightly reduced electric field of 275 kV/mm is applied at 200°C. It is evident that the degradation of U_e and η is well-controlled up to 150°C. Specifically, U_e decreases slightly from 2.69 J/cm³ at room temperature to 2.42 J/cm³ at 150°C, while η decreases from 85.5% to 80.6% over the same temperature range. However, at 200°C, both U_e and η experience a more significant decrease, with U_e dropping to 1.46 J/cm³ and η reducing to 69.4%. It is primarily attributed to the enhanced conduction loss resulting from the significantly reduced breakdown strength. Overall, our optimized anisotropic sample demonstrates

promising performance and applicability for capacitive energy storage at 150°C.

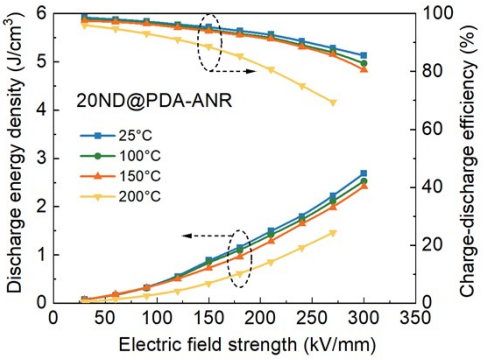

Figure S17. Temperature-dependent energy storage parameters (U_e and η) of 20ND@PDA-ANR.

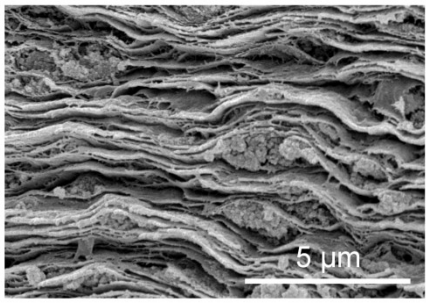

Figure S18. Cross-sectional SEM image of the 20ND@PDA-ANR film after thermal aging at 150°C for 200 h.

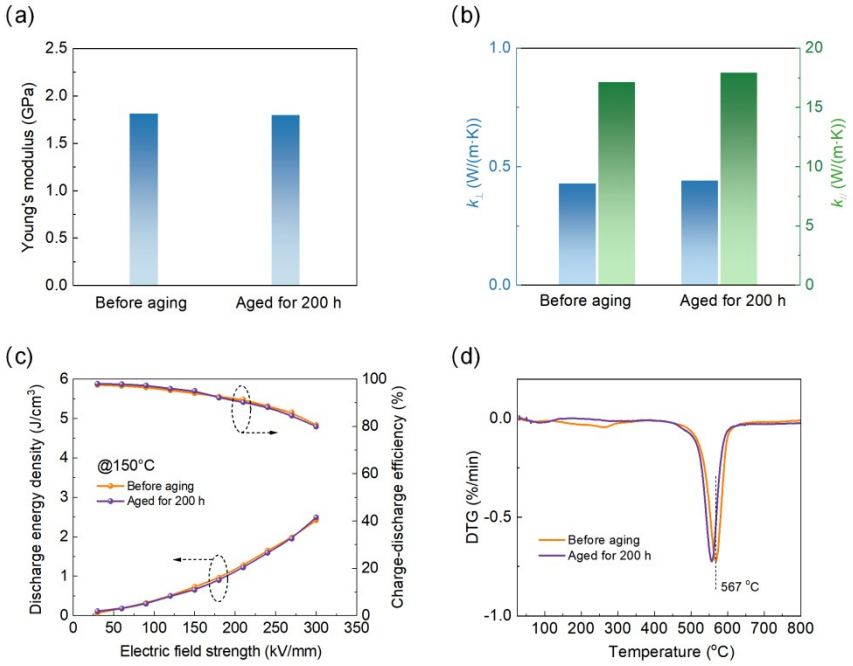

Figure S19. (a) Young's modulus, (b) out-of-plane ($k_{\perp}$) and in-plane ($k_{//}$) thermal conductivity, (c) energy storage parameters, and (d) DTG curves of the 20ND@PDA-ANR film measured before and after the thermal aging process.

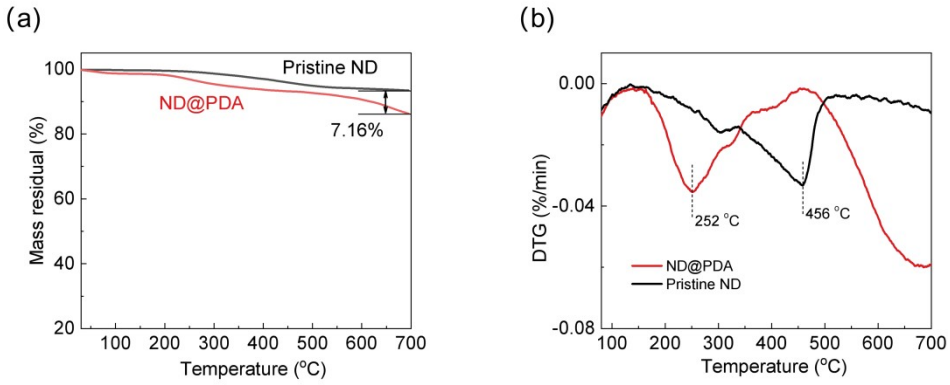

Figure S20. (a) TGA and (b) DTG curves of pristine ND and ND@PDA particles.

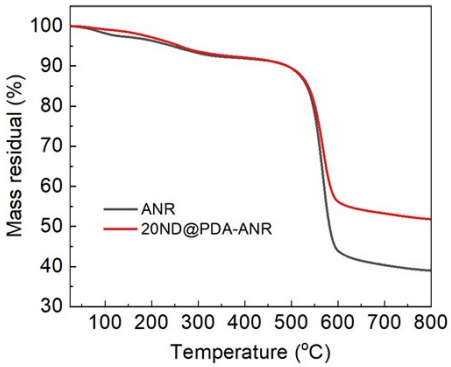

Figure S21. TGA curves of various samples.